CHAPTER-4

Cathodic and anodic reconstruction of Prussian blue analogues during electrochemical water splitting

4.1. Abstract

PBAs form active $M(OH)_2$-M(O)OH nanosheets by an anodic potential-driven electrochemical transformation process. However, the complete reconstruction of PBAs under cathodic potential has never been explored for the alkaline hydrogen evolution as well as overall water splitting. In this chapter, we have explored the cathodic as well as the anodic transformation of self-supported CoFeCo-PBA@CC for the first time by applying cathodic and anodic potentials under CA conditions. Notably, CoFeCo-PBA@CC was reconstructed into two different active catalysts namely Fe-$Co(OH)_2$ (AC-7) and Fe-$Co(OH)_2$-Co(O)OH (AC-9) at cathode and anode, respectively. The active catalysts AC-7 and AC-9 have different structures, thickness as well as Fe-content. The AC-7 has shown enhanced hydrogen evolution activity while AC-9 delivered excellent water oxidation activity in alkaline medium. Interestingly, the outstanding overall water splitting activity has been achieved at 1.58 V cell voltage for 20 mA cm^{-2} current density by coupling of both the active catalysts as anode and cathode.

4.2. Introduction

In this chapter, we have described the electrochemical activation of PBA at the cathode to produce an active catalyst for hydrogen evolution reaction. Although a series of MOFs have been reconstructed electrochemically into $M(OH)_2$-M(O)OH active catalyst driven by anodic potential, the electrochemical reconstruction of MOFs at the cathode has been rarely studied [64]. Still now, the electrochemical reconstruction of FeCoMnNi-MOF was reported to form FeCoMnNi-LDH after applying the cathodic potential [182]. The reconstructed FeCoMnNi-LDH was employed for the overall water splitting in an alkaline medium. Interestingly, the electrochemical reconstruction of PBA under cathodic potential has never been explored [64].

The lacunae in this field led us to investigate the electrochemical reconstruction of self-supported PBAs under anodic as well as cathodic potential by the CA method. For this purpose, we have developed self-supported CoFeCo-PBA (PC-4) (Figure 4.1). Further, the PC-4 was used for electrochemical transformation under CA conditions to form two different active catalyst structures at the cathode and anode (Figure 4.1). Further, the CoCo-PBA (PC-5) was also synthesized and reconstructed under similar conditions to form the active catalysts for comparison purposes. The specific objectives of this chapter are described below:

(i) The self-supported CoFeCo-PBA precatalyst (PC-4) was developed using a cobalt iron hydroxide template. The CoCo-PBA (PC-5) was also prepared to understand the effect of Fe doping in the PBA precatalysts.

(ii) The electrochemical bulk reconstruction of PC-4 and PC-5 has been accomplished under the CA conditions by applying the anodic as well as cathodic potential. The effect of anodic and cathodic potential on the active catalyst structure has been investigated with the help of spectroscopic and microscopic techniques.

(iii) The electrochemically reconstructed anodic active catalyst was implemented for electrochemical OER while the cathodically formed active catalyst was employed for the electrochemical HER. In addition, the coupling of the anodic and cathodic active catalysts has also been performed to establish an overall water-splitting system. The role of Fe doping in the active catalysts has been well established to improve the OER as well as HER activity.

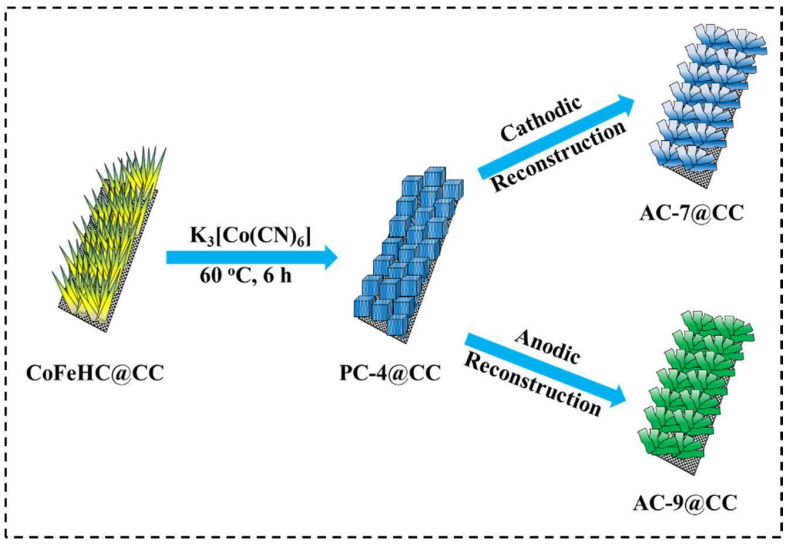

Figure 4.1. Schematic representation for the synthesis of PC-4 precatalyst from CoFeHC@CC template and their electrochemical reconstruction at cathode and anode to form active catalysts AC-7 and AC-9, respectively.

4.3. Chemicals

All the chemicals were utilized similar to chapter 2 (section 2.3). $K_3[Co(CN)_6]$ was obtained from SRL India Pvt. Ltd.

4.4. Instruments

The instruments were described in chapter 2 (section 2.4).

4.5. Experimental

4.5.1. Synthesis of cobalt iron hydroxide on carbon cloth (CoFeHC)

For the synthesis of CoFeHC, 1 mmol of each $CoCl_2.6H_2O$ and $FeCl_2.4H_2O$ were added to the 12 mL of H_2O. Further, 4 mmol NH_4F and 10 mmol of NH_2CONH_2 were added to the above mixture. The mixture was taken in a Teflon-lined autoclave and the pieces of CC were dipped vertically inside the autoclave. Further, the autoclave was put in a preheated oven for 5 h at 120 ℃. After natural cool down, the films of CoFeHC@CC were washed with H_2O and ethanol three times and subsequently dried in an oven for 12 h at 50 °C. The CoHC@CC was prepared similar to chapter 2 (section 2.5).

4.5.2. Synthesis of PC-4 and PC-5

A solution of $K_3[Co(CN)_6]$ (0.2 mmol) was prepared in 5 mL of H_2O and taken into a screw-capped vial. Further, one piece of CoFeHC@CC was set vertically inside the vial and aged at RT for 1 h. Further, the vial was capped and put in a preheated air oven for 6 h at 60 ℃. A brown color PBA was deposited on carbon cloth. After normal cool down, the PBA film was taken out from the vial and washed thoroughly with H_2O several times and further drying was performed in an oven for 12 h at 50 ℃. The fresh PC-4 films were employed as working electrodes for the electrochemical reconstruction. Similarly, CoCo-PBA (PC-5) was also prepared by treating the CoHC@CC template with $K_3[Co(CN)_6]$ under a similar reaction condition.

4.5.3. Synthesis of CoHC@CC, FeHC@CC, and CoFe-LDH@CC

For comparison purposes, CoHC@CC and CoFe-LDH@CC were hydrothermally synthesized as mentioned in chapter 2 (section 2.5). For the synthesis of FeHC@CC, the $CoCl_2.6H_2O$ was replaced by $FeCl_2.4H_2O$.

4.5.4. Electrochemical measurements

Electrochemical measurement details were also mentioned in chapter 2 (section 2.6).

4.6. Results and discussion

4.6.1. Characterization of precatalysts PC-4 and PC-5

The FTIR spectra of PC-4 and PC-5 detected the prominent peaks at 2200 cm^{-1} and 2070 cm^{-1}, which were ascribed to the asymmetric stretching vibration of bridging –CN groups in PBA (Figure 4.2a) [266]. The PXRD pattern evidenced the cubic crystal system in PC-4 and PC-5 having an *Fm3m* (225) space group (JCPDF No-01-077-1161) (Figure 4.2b).

The XPS studies were performed for the evaluation of the electronic states of elements. The two peaks at 797.2 eV and 781.8 eV were specified in Co 2p XPS of PC-4, assigned to Co $2p_{1/2}$ and Co $2p_{3/2}$, respectively (Figure 4.2c) [65,81,152,229]. The peaks were identified for the mixed valent Co^{2+} and Co^{3+}. Further, spin-orbit coupling spacing of 15.4 eV was evaluated justifying the existence of both Co^{2+} and Co^{3+} in PC-4. The Fe 2p XPS of PC-4 validated the peaks for the existence of only Fe^{3+} (Figure 4.2d) [192,267–269]. The N 1s spectrum evidenced a clear peak at 398.6 eV for the –CN bond in PC-4 (Figure 4.2e) [81,231,270,271]. The two peaks were also fitted in the O 1s spectrum of PC-4 at 530.5 eV (surface –OH) and 531.6 eV (adsorbed H_2O), respectively (Figure 4.2f) [65,81,86,104,152].

Further, SEM studies unveiled the cubic morphology of the PC-4 precatalysts, which was also verified from the TEM images (Figure 4.2g-h). HRTEM image recognized the d-spacing value of 0.50 nm associated with the (200) plane of PC-4 (Figure 4.2i). Similarly, SEM and TEM images identified the cubic shape of PC-5 with a d-spacing value of 0.50 nm (Figure 4.2j-l).

4.6.2. Electrochemical reconstruction of PC-4 and PC-5

The PC-4 was implemented as the working electrode in a single-cell setup with a three-electrode system.

(i) The cathodic reconstruction was carried out using PC-4 as a precatalyst by applying the cathodic potential of -0.2 V *vs* RHE. The cathodic reconstruction rendered the new active catalyst Fe-$Co(OH)_2$ (AC-7) at the cathode. To investigate the effect of Fe-doping,

PC-5 was also reconstructed under similar reaction conditions to form active catalyst $Co(OH)_2$ (AC-8) at the cathode.

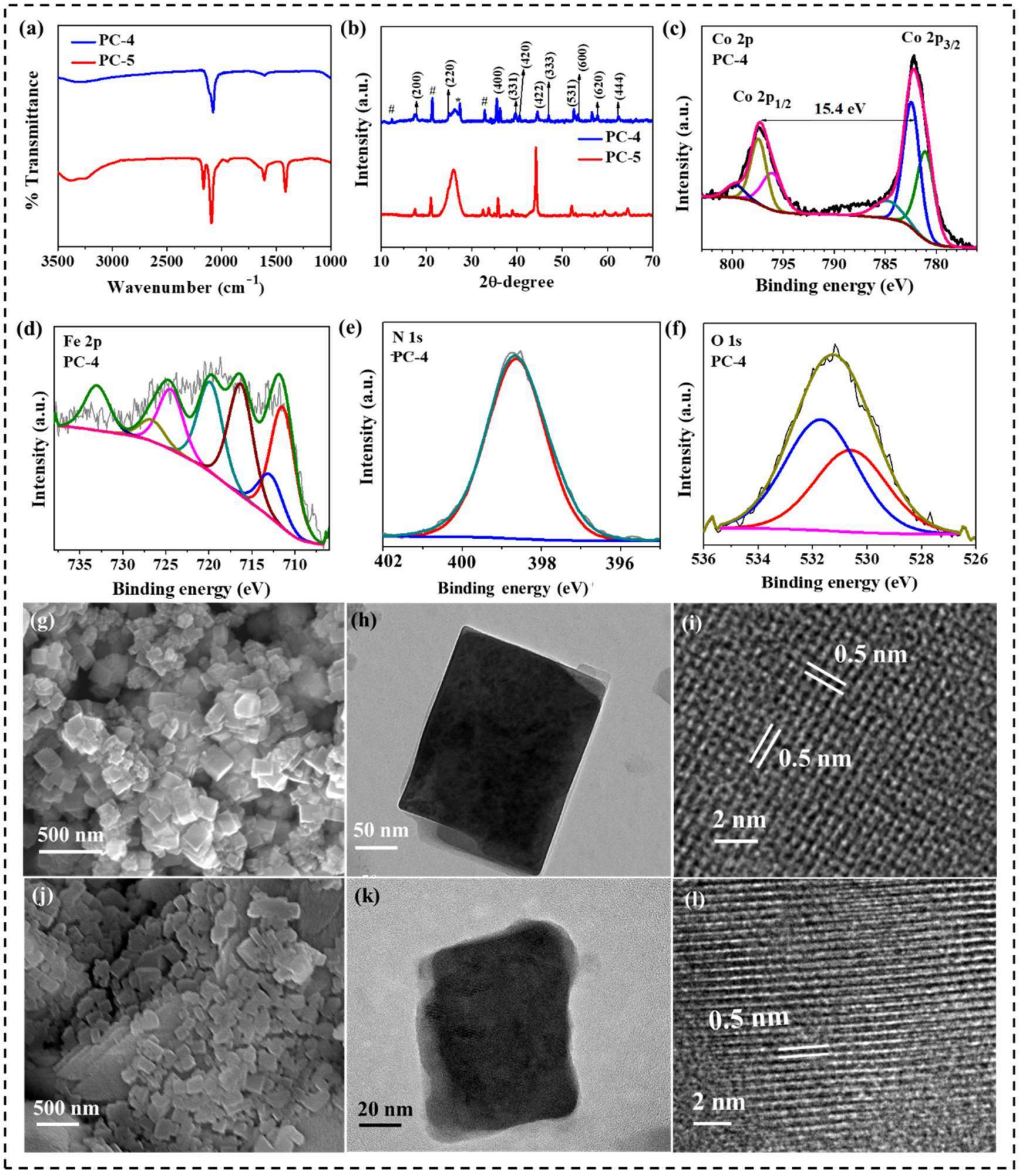

Figure 4.2. (a) IR spectra of PC-4 and PC-5; (b) PXRD pattern of PC-4 and PC-5; (c) Co 2p XPS of PC-4; (d) Fe 2p XPS of PC-4; (e) N 1s XPS of PC-4; (f) O 1s XPS of PC-4; (g) SEM image of PC-4; (h) TEM image of PC-4; (i) HRTEM image of PC-4; (j) SEM image of PC-5; (k) TEM image of PC-5 and (l) HRTEM image of PC-5.

(ii) The anodic reconstruction of PC-4 was performed by applying the potential of 1.50 V *vs* RHE potential. This resulted in the Fe-$Co(OH)_2$-Co(O)OH active catalyst (AC-9) at the anode. For comparison purposes, PC-5 was also reconstructed to form $Co(OH)_2$-Co(O)OH active catalyst at the anode (AC-10).

Table 4.1. Details of the synthesis of reconstructed active catalysts by CA treatment of PC-4 and PC-5.

Precatalyst	Active catalyst	Denoted name	Reaction conditions
PC-4	Fe-$Co(OH)_2$	AC-7	-0.2 V *vs* RHE, CA
PC-5	$Co(OH)_2$	AC-8	-0.2 V *vs* RHE, CA
PC-4	Fe-$Co(OH)_2$-Co(O)OH	AC-9	1.50 V *vs* RHE, CA
PC-5	$Co(OH)_2$-Co(O)OH	AC-10	1.50 V *vs* RHE, CA

4.6.3. Characterization of the cathodic active catalyst AC-7

In contrast to the anodic catalyst, the cathodic reconstruction of PC-4 led to the formation of a new active catalyst with a Fe-doped $Co(OH)_2$ structure. IR and Raman spectra identified the disappearance of the peak for bridged –CN groups after the cathodic reconstruction (Figure 4.3a-b) [64,178]. The PXRD pattern of AC-7 evidenced the mixed phase structure of α-$Co(OH)_2$ (JCPDF No-02-0925) and β-$Co(OH)_2$ (JCPDF No-45-0031) in AC-7 (Figure 4.3c).

Further, the Co 2p XPS exhibited two peaks at 796.0 eV and 780.7 eV supporting the existence of Co^{2+} species to form Fe-doped Co-hydroxide in AC-7 (Figure 4.3d) [272]. The AC-7 demonstrated the spin-orbit coupling spacing of 15.3 eV while a slight change in the value of peaks was evidenced in Co 2p XPS in contrast to the PC-4. In Fe 2p XPS of AC-7, the peaks were identified for the Fe^{2+} and Fe^{3+} species (Figure 4.3e) [230]. After the cathodic transformation, O 1s XPS realized the peaks at 529.7 eV for the metal-oxygen bond, 530.8 eV for surface –OH, and 532.5 eV for adsorbed H_2O (Figure 4.3f) [65,81]. ICP-AES studies detected 73% of Fe in the active catalyst AC-7 after the reconstruction. This concluded that the amount of Fe leaching was less in the cathodic

transformation compared to the anodic transformation. Although the SEM image specified the agglomeration of the ultrathin nanosheets of AC-7 after cathodic transformation (Figure 4.3g) but TEM image verified the ultrathin transparent nanosheets (Figure 4.3h). HRTEM image corroborated the 0.24 nm lattice spacing related to the (101) plane in β-$Co(OH)_2$ (JCPDF No-45-0031) (Figure 4.3i). SAED pattern revealed the two planes (201) and (101) for α-$Co(OH)_2$ and β-$Co(OH)_2$, respectively (Figure 4.3i inset). Interestingly, the thickness of AC-7 was analyzed to be ~3 nm from AFM studies (Figure 4.3j).

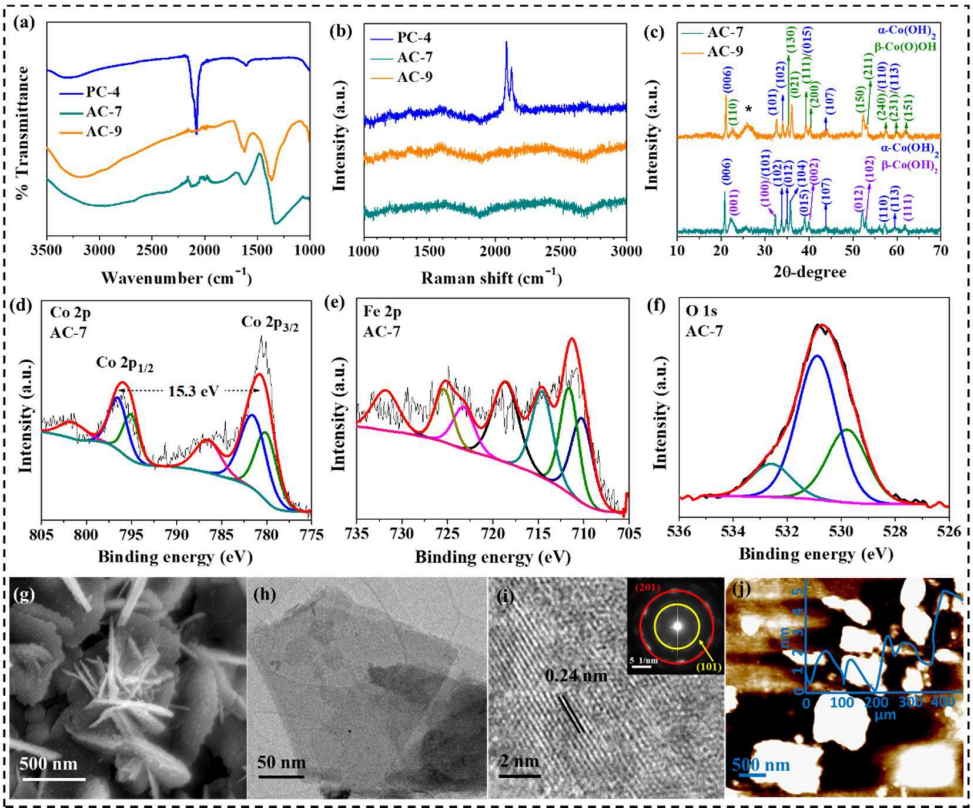

Figure 4.3. (a) IR spectra of AC-7 and AC-9 compared with PC-4; (b) Raman spectra of AC-7 and AC-9 compared with PC-4; (c) PXRD pattern of AC-7 and AC-9; (d) Co 2p XPS of AC-7; (e) Fe 2p XPS of AC-7; (f) O 1s XPS of AC-7; (g) SEM image of AC-7; (h) TEM image of AC-7; (i) HRTEM image of AC-7 (SAED inset) and (j) AFM image of AC-7 (height profile inset).

4.6.4. Characterization of the anodic active catalyst AC-9

The electrochemical reconstruction of PC-4 also rendered the Fe-doped α-$Co(OH)_2$-β-Co(O)OH (AC-9) catalyst at the anode similar to the previous chapters. The IR and Raman spectra showed no evidence for the peak of bridging –CN groups (Figure 4.3a-b) [81,178]. The PXRD pattern evidenced that the AC-9 possessed two different phases of α-$Co(OH)_2$ (JCPDF No-02-0925) and β-Co(O)OH (JCPDF No-26-0480) (Figure 4.3c).

The prominent peaks at 795.6 eV and 780.6 eV were evidenced for the Co $2p_{1/2}$ and $2p_{3/2}$ in the Co 2p XPS of AC-9, respectively (Figure 4.4a) [81,178]. A significant lowering in the spin-orbit coupling spacing (15.1 eV) was determined in contrast to the PC-4 (15.4 eV) suggesting the high content of Co^{3+} in AC-9 [81,178]. The Fe 2p XPS peaks validated the presence of Fe^{2+} and Fe^{3+} in AC-9 (Figure 4.4b) [65,178]. Further, the O 1s XPS identified the characteristic peaks at 530.4 eV (surface –OH) and 532.11 eV (adsorbed H_2O) whereas the peak at 529.4 eV was corroborated with the metal-oxygen bonds in AC-9 (Figure 4.4c) [64,65,178].

Similar to the previous chapters, ICP-AES studies detected the leaching of Fe from PC-4 during the CA transformation where only 14% of Fe was found in AC-9 [64,65,178]. SEM studies realized the ultrathin nanosheets overlapped to form flower-like morphology (Figure 4.4d). TEM image verified the ultrathin nanosheets after the anodic transformation (Figure 4.4e). Further, the HRTEM image of AC-9 specified the lattice spacing value of 0.23 nm associated with the (111) plane of β-Co(O)OH (JCPDF No-26-0480) (Figure 4.4f). SAED pattern of AC-9 was related to the (201) and (111) plane in α-$Co(OH)_2$ and β-Co(O)OH, respectively (Figure 4.4f inset). AFM was also analyzed for AC-9 indicating the ~6 nm thickness (Figure 4.4g).

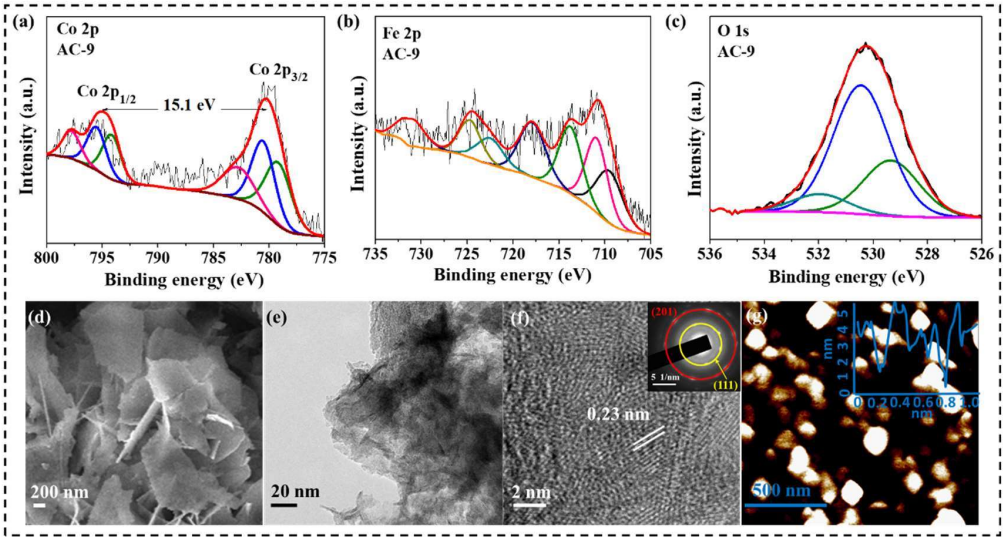

Figure 4.4. (a) Co 2p XPS of AC-9; (b) Fe 2p XPS of AC-9; (c) O 1s XPS of AC-9; (d) SEM image of AC-9; (e) TEM image of AC-9; (f) HRTEM image of AC-9 (SAED inset) and (g) AFM image of AC-9 (height profile inset).

4.6.5. Electrochemical performance

The cathodically synthesized catalyst AC-7 was employed for the effective hydrogen evolution reaction. The AC-7 demonstrated excellent HER activity in contrast to the AC-8. Interestingly, AC-7 afforded -10 mA cm^{-2} cathodic current density only at the input of 155 mV overpotential (Figure 4.5a). The AC-7 offered more impressive HER activity than the self-supported transition metal-based catalysts as well as the electrocatalysts developed from PBA. The LSV profiles revealed that the Fe-introduction drastically improved the HER activity for AC-7 compared to AC-8 (Figure 4.5a). The Tafel slope of 60 mV dec^{-1} was evaluated for AC-7 in contrast to AC-8 (Figure 4.5b). Further, AC-7 realized the excellent durability of 50 h under CA measurements for electrochemical HER (Figure 4.5c).

The anodically reconstructed AC-9 and AC-10 catalysts were implemented for the electrochemical OER. The CV profile manifested the best OER activity for AC-9, which

demonstrated only 220 mV overpotential to afford 10 mA cm^{-2} current density (Figure 4.5d). In contrast, AC-10 afforded the anodic current density of 10 mA cm^{-2} at 260 mV overpotential. The electrochemically reconstructed AC-9 outperformed the noble metal-based RuO_2 catalyst for oxygen evolution (Figure 4.5d). The CV profiles validated the remarkable OER activity of electrochemically derived AC-9 in contrast to the hydrothermally synthesized bulk CoHC, FeHC, and CoFeHC (Figure 4.5d). Further, the Tafel slope of AC-9 was analyzed to be 55 mV dec^{-1} smallest among the synthesized electrocatalysts demonstrating the faster OER kinetics (Figure 4.5e). The long-term stability of AC-9 was assessed for 50 h under CA conditions (Figure 4.5f). It should be clarified that the introduction of Fe in hydrothermally prepared CoHC as well as in PC-4 impressively improved the activity of the CoFeHC and reconstructed AC-7 and AC-9 catalysts [273,274].

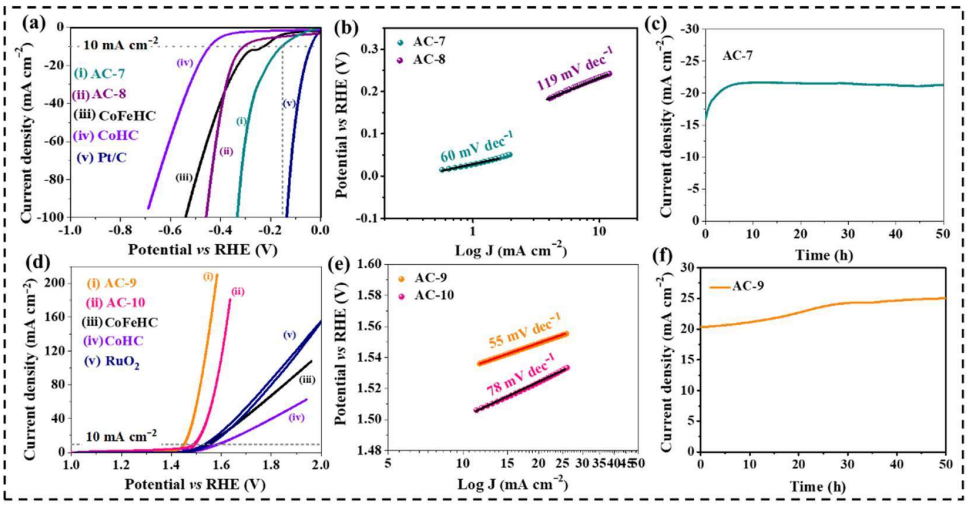

Figure 4.5. (a) LSV profile for the HER activity of AC-7, AC-8, CoFeHC, CoHC, Pt/C; (b) Tafel plots of AC-7 and AC-8; (c) HER-CA stability test of AC-7 for 50 h at -0.2 V *vs* RHE; (d) CV profiles for the OER activity of AC-9, AC-10, CoFeHC, CoHC, RuO_2; (e) Tafel plots of AC-9 and AC-10 and (f) OER-CA stability test of AC-9 for 50 h at 1.50 V *vs* RHE.

Owing to the excellent OER and HER activity of the electrochemically derived active catalysts, the cathodic (AC-7) and anodic (AC-9) catalysts were coupled to achieve the overall water-splitting activity in an alkaline medium (Figure 4.6a). Interestingly, the overall water splitting was recorded at the cell potential of 1.58 V to afford the current density of 20 mA cm^{-2} (Figure 4.6b). The durability of the active catalysts was examined by CA, which unveiled the 30 h stability for the overall water splitting (Figure 4.6b inset). The overall water splitting activity was recorded to be outstanding among the previously reported transition metal-based catalysts. Further, the FE was estimated to be 95% for the overall water splitting.

The EIS spectra specified the lower charge transfer kinetics of electrochemically derived AC-9 compared to the AC-10 and hydrothermally prepared CoFeHC bulk (Figure 4.6c). Further, ECSA was analyzed by the C_{dl} measurement. The ECSA of 37.00 cm^2 was determined for AC-9, which was larger than that of AC-10 (6.25 cm^2) (Figure 4.6d). The larger ECSA clarified the larger exposed active sites, which expedited the water binding to promote the performance.

4.7. Conclusions

In conclusion, we have demonstrated the synthesis of new CoFeCo-PBA@CC (PC-4) on carbon cloth. CoCo-PBA (PC-5) was also synthesized to realize the effect of Fe doping. The PC-4 and PC-5 were implemented for the electrochemical reconstruction to form different active catalyst structures at the cathode and anode. The PC-4 rendered the cathodic Fe-$Co(OH)_2$ (AC-7) catalyst and anodic Fe-$Co(OH)_2$-Co(O)OH (AC-9) catalyst while PC-5 generated cathodic $Co(OH)_2$ (AC-8) and anodic $Co(OH)_2$-Co(O)OH (AC-10) catalysts, respectively. The thickness of the cathodic catalyst was analyzed to be ~3 nm while the anodic catalyst realized ~6 nm thickness. Interestingly, AC-9 offered a remarkable OER overpotential of 220 mV delivering a current density of 10 mA cm^{-2}.

Furthermore, HER activity of AC-7 was also recorded at 155 mV overpotential for -10 mA cm^{-2} cathodic current density. The overall water splitting activity was also established at 1.58 V cell potential affording 20 mA cm^{-2} current density. Moreover, the CA stability of 30 h was also realized for excellent overall water splitting.

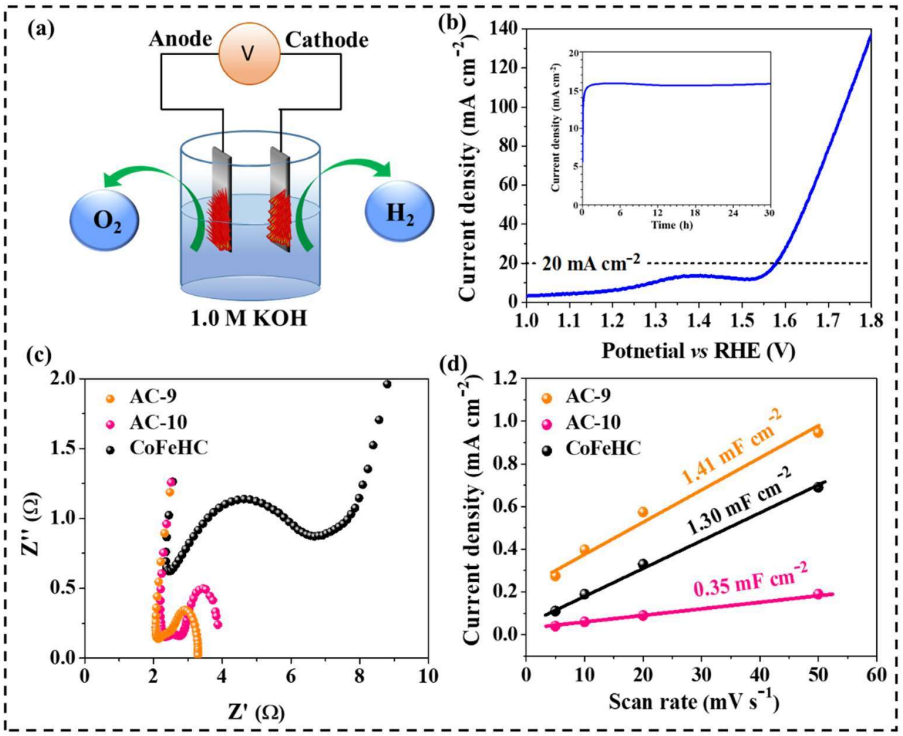

Figure 4.6. (a) Schematic illustration for the overall water splitting in a two electrode electrolyzer cell; (b) LSV profile for the overall water splitting activity by the coupling of AC-7 and AC-9 at anode and cathode, respectively (inset CA test for 30 h); (c) EIS plot of AC-9, AC-10, CoFeHC; and (d) C_{dl} plot of AC-9, AC-10, CoFeHC.